Lithium sulfur battery exploiting material design and electrolyte chemistry: 3D graphene framework and diglyme solution

Almudena Benítez[a], Daniele Di Lecce[b], Álvaro Caballero[a], Julián Morales[*,a], Enrique Rodríguez-Castellón[c], and Jusef Hassoun[*,b,d]

[a]*Dpto. Química Inorgánica e Ingeniería Química, Instituto de Química Fina y Nanoquímica, Universidad de Córdoba, 14071 Córdoba, Spain.*

[b]*Department of Chemical and Pharmaceutical Sciences, University of Ferrara, Via Fossato di Mortara, 17, 44121, Ferrara, Italy.*

[c]*Dpto. de Química Inorgánica, Cristalografía y Mineralogía, Facultad de Ciencias, Universidad de Málaga, 29071 Málaga, Spain.*

[d] *National Interuniversity Consortium of Materials Science and Technology (INSTM) University of Ferrara Research Unit, University of Ferrara, Via Fossato di Mortara, 17, 44121, Ferrara, Italy.*

*Corresponding authors: iq1mopaj@uco.es, jusef.hassoun@unife.it

Abstract

Herein we investigate a lithium sulfur battery suitably combining alternative cathode design and relatively safe, highly conducting electrolyte. The composite cathode is formed by infiltrating sulfur in a N-doped 3D graphene framework prepared by a microwave assisted solvothermal approach, while the electrolyte is obtained by dissolving lithium bis(trifluoromethane)sulfonimide (LiTFSI) in diethylene glycol dimethyl ether (DEGDME), and upgraded by addition of lithium nitrate ($LiNO_3$) as a film forming agent. The particular structure of the composite cathode, studied in this work by employing various techniques, well enhances the lithium-sulfur electrochemical process leading to very stable cycling trend and specific capacity ranging from 1000 mAh g^{-1} at

the highest rate to 1400 mAh g^{-1} at the lowest one. The low resistance of the electrode/electrolyte interphase, driven by an enhanced electrode design and a suitable electrolyte, is considered one of the main reasons for the high performance which may be of interest for achieving a promising lithium-sulfur battery. Furthermore, the study reveals a key bonus of the cell represented by the low flammability of the diglyme electrolyte, while comparable conductivity and interface resistance, with respect to the most conventional solution used for the lithium sulfur cell.

Keywords

3D-graphene; Li-S battery; solvothermal microwave; nitrogen doping; low flammability.

1. Introduction

Continuously increasing energy demand leads to fossil fuels depletion with emission of greenhouse gases and pollutants, as well to concerns on possible climate changes [1,2]. Hence, relevant research is now devoted towards the development of sustainable energy-storage systems for renewable sources and electric engines, such as the advanced lithium batteries [3]. Among them, the lithium-sulfur battery is one of the most attractive systems due to the remarkable energy density ensured by a multi-electron process delivering a theoretical specific capacity of 1675 mAh g^{-1} and occurring at about 2.1 V [4]. Therefore, the lithium-sulfur battery has a theoretical energy density of about 3600 Wh kg^{-1} (2600 Wh kg^{-1} referred to Li_2S), that is, almost one order of magnitude higher than that of conventional lithium-ion batteries [4–6]. However, this interesting system suffers from several drawbacks [7–9], such as the insulator character of the sulfur, the dissolution of polysulfides intermediates (Li_2S_x, $4 \leq x \leq 8$) into the electrolyte during the electrochemical process, and their shuttle from the cathode to the anode leading to short-circuit and cell degradation [4]. Accordingly, the incorporation of sulfur into conductive carbonaceous matrixes has been widely investigated to ensure high current rates, and

mitigate the polysulfide dissolution upon cycling [10–14]. Carbon materials with various structures, morphologies and porosities have been studied [12,14–17], including graphitic oxide (GO) and graphenes [18,19]. The use of carbon interlayers between separator and cathode as well as the design of advanced electrodes formed by elemental sulfur entrapped within carbon-nanotube-based scaffolds can inhibit the polysulfide dissolution and improve the cycle life [20]. Thus, separator modification by metal organic frameworks and multilayer cathode engineering have proven to enhance the cell performance, even in the lithium-ion configuration [21–23]. Furthermore, disordered conductive frameworks with controlled pore size distribution have been obtained by staking graphene within a three-dimensional (3D) array [24], and proposed to accommodate sulfur for ensuring fast charge transfer with limited polysulfides dissolution [25,26]. Nitrogen incorporation in graphene foams has proven to limit the shuttle effect due to polysulfides adsorption over the carbon surface by pyridinic and pyrrolic functional groups [27,28], and to increase the electronic conductivity of graphene [29]. Possible strategy to protect the lithium-metal anode involves the formation of stable, lithium-ion conductive solid electrolyte interphase (SEI) by the addition of film-forming agents to the electrolyte solution [30,31]. Thus, remarkable performances have been achieved by adding $LiNO_3$ to a solution formed by dissolving LiTFSI in 1,3-dioxolane (DOL) and dimethyl ether (DME) [32–34]. Despite the relevant ionic conductivity and the suitable SEI formation [33], this electrolyte suffers from a safety issue ascribed to the use of highly-flammable solvents. Glyme-based solutions are characterized by a lower flammability which allows their relatively safe use in lithium metal battery and, therefore, in Li-S cell [35,36]. However, the glyme with chemical formula $CH_3(OCH_2CH_2)_nOCH_3$ reveals higher viscosity than DOL and DME, thus lower conductivity and higher electrode/electrolyte interface resistance, in particular by increasing n values [35,36]. A careful optimization of the electrolyte formulation is a crucial step to improve its

stability, prevent the lithium dendrite growth, and avoid parasitic reduction of the dissolved lithium polysulfide at the anode side upon charge, thereby leading to enhanced performance and prolonged cycle life [4,37]. Accordingly, we have lately reported a comparative study of glyme-based electrolytes for lithium-sulfur batteries, which suggested solutions using the short-chain diethylene glycol dimethyl ether (DEGDME, n = 2) and dissolving 0.4 mol kg^{-1} $LiNO_3$, in view of a beneficial combination of suitable thermal stability, low viscosity, high conductivity and interface stability leading to promising cell behavior [35]. Following this trend, we have optimized and thoroughly characterized in a subsequent work a DEGDME-LiTFSI solution containing 1 mol kg^{-1} of $LiNO_3$, thereby demonstrating improved reversible capacity and cycling stability [38].

Herein, we further enhance the lithium-sulfur cell by employing a composite cathode formed by elemental sulfur hosted in a 3D, N-doped graphene (3DNG-S) matrix [39,40] and the electrolyte solution combining DEGDME solvent with LiTFSI and $LiNO_3$ salts both in the 1 mol kg^{-1} concentration. Structure, morphology, composition, and surface functional groups of the 3DNG-S cathode are carefully studied. Upon characterization of the electrochemical stability, rate capability, energy density and safety content, in terms of electrolyte flammability, we suggest the novel Li-S cell as sustainable high-energy storage system benefiting from the synergistic properties of cathode and electrolyte.

2. Experimental

2.1 Preparation of 3D N-doped graphene–sulfur composite (3DNG-S)

Graphite oxide precursor (GO) was synthesized from flaky graphite powder by a modified Hummers method [41]. Briefly, 3 g of graphite powder (Merck), 70 mL of H_2SO_4 (98 %, Panreac) and 1.5 g of $NaNO_3$ (Sigma Aldrich) were put into a 1000 mL graduated beaker and stirred continuously in ice bath for 20 min. Then, an amount of 9 g

of potassium permanganate was slowly added, and the solution was stirred in ice bath to keep the temperature lower than 20 ºC. Afterwards, the solution was stirred in water bath at 35-40 ºC for 30 min, further promoting the oxidation of graphite (mesothermal reaction stage). A volume of 140 ml of deionized water was added, and the suspension was heated up to 95 ºC for 15 min (hyperthermal reaction stage). At the end of the hyperthermal reaction stage, 500 mL of deionized water was added. Therefore, a volume of 15 ml of H_2O_2 solution in water (3 %, Sigma Aldrich) was slowly added to the suspension to obtain a dark brown gel. The product was filtered, centrifuged, and washed with 250 mL of a 10 % aqueous solution of HCl (37 %, Panreac). Then, the gel was washed until neutral pH to obtain GO suspension, which was dried at 60 ºC into an oven during 12 h.

N-doped graphene was obtained via microwave-assisted exfoliation and reduction of GO by using urea as a nitrogen source. Typically, a volume of 40 ml of an aqueous suspension of GO (2 mg ml^{-1}) was dispersed through ultrasonication for 1 h, and then added with 370 mg of urea [42]. The suspension was transferred into a 100 ml Teflon-lined autoclave and put into a microwave oven (Milestone flexiWAVE) at power of 350 W and temperature of 200 ºC for 12 h [43]. The autoclave was naturally cooled to obtain a carbon monolith which was dipped into distilled water, filtered and washed several times to remove the residual salts, and freeze-dried (Telstar Lyo Quest, Mod. 85) to obtain the 3D N-doped graphene (3DNG) monolithic sponge. The synthesis pathway of the 3DNG from graphite is schematically described in Fig. 1.

3D N-doped graphene was mixed with 100 ml of deionized water and 10 ml of dry absolute ethanol (Panreac), and then sonicated for 30 min to get a dispersion. A quantity of 200 mg of sublimed sulfur (VWR Chemical) was added into 10 ml of anhydrous ethylenediamine (Sigma Aldrich) to form a sulfur-amine precursor solution, which was then drop-wisely added into the dispersion in 3 min under magnetic stirring

[39]. The suspension was continuously stirred for 10 min, filtered, rinsed and dried at 50 °C to obtain the 3D N-doped graphene–sulfur (3DNG-S) composite.

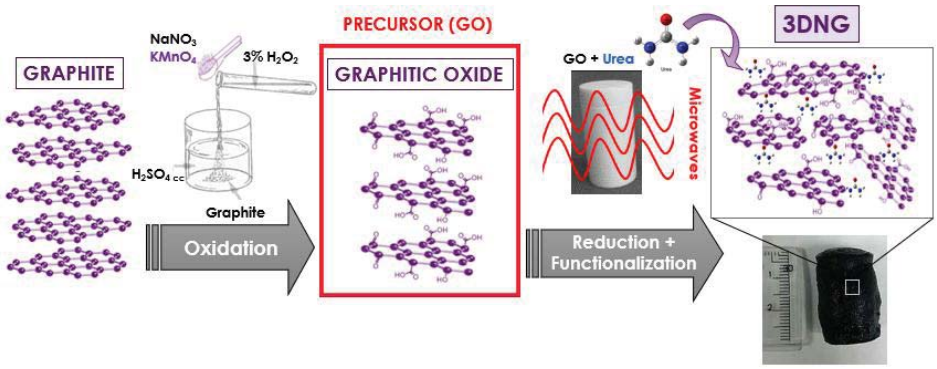

Figure 1. Synthesis pathway of the 3DNG-S material, including a photograph of the 3DNG-S monolith after the microwave-assisted solvothermal treatment. See experimental section for samples' acronym.

2.2 Preparation of DEGDME-LiTFSI electrolyte

Diethylene glycol dimethyl ether (DEGDME, anhydrous, $(CH_3OCH_2CH_2)_2O$, Sigma-Aldrich) was dried under molecular sieves (5 Å, Sigma-Aldrich) until the water content was below 10 ppm, as determined by 899 Karl Fischer Coulometer, Metrohm. Lithium bis(trifluoromethane)sulfonimide (LiTFSI, Sigma-Aldrich) and lithium nitrate ($LiNO_3$, Sigma-Aldrich) were dried under vacuum at 110 and 80 °C, respectively, for 3 days. The electrolyte was prepared by dissolving 1 mol of $LiNO_3$ and 1 mol of LiTFSI in 1 kg of DEGDME, and indicated by the acronym DEGDME-LiTFSI-$LiNO_3$.

A reference electrolyte formed following the same procedure, using as the solvents 1,3-dioxolane (DOL, anhydrous, $C_3H_6O_2$, Sigma-Aldrich), and 1,2-dimethoxyethane (DME, anhydrous, $CH_3OCH_2CH_2OCH_3$, Sigma-Aldrich) with 1:1 weight ratio was prepared and indicated with the acronym DOL:DME-LiTFSI-$LiNO_3$. The electrolytes preparation was carried out in an argon-filled glove-box with moisture and oxygen content lower than 1 ppm.

2.3. Materials characterization

XRD patterns were recorded with a Bruker D8 Discover X-ray diffractometer using monochromatic Cu K_α radiation. The patterns were acquired within the 5 – 80º (2θ) range, using a step size of 0.015º and 0.1 s per step. Raman measurements were carried out with a Renishaw inVida Microscope equipped with a detector Renishaw CCD Camera (578 x 400) and a laser of 532 nm edge in line focus mode. The sulfur content was determined by thermogravimetric analysis with a Mettler Toledo-TGA/DSC under nitrogen atmosphere, heating the sample from 25 to 600 ºC at 5 ºC min^{-1}. Samples morphology was examined by a Zeiss EVO 40 and a Jeol JSM-7800F scanning electron microscopes (SEM). Energy dispersive X-ray spectra (EDS) were recorded through the microanalysis system of the latter microscope. CHN analysis were carried out by EuroVector EA-3000. X-ray photoelectron spectroscopy (XPS) was performed through a Physical Electronics PHI 5700 spectrometer, using monochromatic Mg K_α radiation and a multichannel detector. All spectra were fitted to Gauss–Lorentz curves in order to better identify the different functional group in each material. Specific surface areas were determined with a Quantachrome Instruments Autosorb iQ/ASiQwin, using N_2 gas as adsorbate. Pore size distribution was calculated by the density functional theory (DFT) method applied to the adsorption branch of the isotherms.

Flammability tests were carried out on DEGDME-LiTFSI-$LiNO_3$ electrolyte and DOL:DME-LiTFSI-$LiNO_3$ reference sample through direct contact with a butane flame, by changing the exposure time for the various samples of each electrolyte.

2.4. Cathode preparation, cell assembly and electrochemical characterization

The positive electrode was prepared by mixing the active material with a polymer binder (PVDF 6020, Solvay) and a conducting agent (Super P carbon, Timcal) according to the weight proportion of 80:10:10, and dispersing in agate mortar using a 1-methyl-2-

pyrrolidone (NMP, Sigma Aldrich) solvent to form a dense, homogeneous slurry. The slurry was coated by doctor blade deposition on a gas diffusion layer (GDL ELAT LT1400) [44]. The electrode foil was dried for 3 hours at 60 °C by using a hot-plate and cut into 14-mm disks (1.54 cm^2 geometric surface). Then, the electrode was dried under vacuum overnight at 45 ºC. The active material loading was between 2.0 – 2.8 mg_S cm^{-2}.

Electrochemical measurements were performed on CR2032 coin-cells assembled inside an Ar-filled glovebox (MBraun, oxygen and moisture content lower than 1 ppm). A polyethylene membrane (Celgard) separator was used for all the electrochemical tests except the conductivity measurements. The ionic conductivities of DEGDME-LiTFSI-$LiNO_3$ electrolyte and DOL:DME-LiTFSI-$LiNO_3$ reference were measured at room temperature by electrochemical impedance spectroscopy (EIS) on symmetrical stainless steel/stainless steel (SS/SS) cells employing a Teflon ring as the separator to fix the cell constant (4.0×10^{-2} cm^{-1}). EIS were carried out by applying an alternate voltage signal of 10 mV amplitude within the 500 – 1 kHz frequency range. Further EIS measurements were also performed on two symmetrical Li/Li cells using DEGDME-LiTFSI-$LiNO_3$ electrolyte and DOL:DME-LiTFSI-$LiNO_3$ reference, respectively, by applying an alternate voltage signal of 10 mV amplitude within the 500 kHz – 1 Hz frequency range.

Li/DEGDME-LiTFSI-$LiNO_3$/3DNG-S cells were assembled and studied by cyclic voltammetry (CV) and galvanostatic cycling. CV was performed at a scan rate of 0.1 mV s^{-1} within the 1.8 – 2.8 V range. EIS spectra were recorded at the open circuit voltage (OCV) condition, after 6 and after 12 CV cycles, by applying an alternate voltage signal of 10 mV amplitude within the 500 kHz – 0.1 Hz frequency range. The CV and all the EIS measurements were carried out through a VersaSTAT MC Princeton Applied Research (PAR, AMETEK) analyzer. Galvanostatic cycling tests were carried within the 1.9 – 2.8 V range with a MACCOR series 4000 battery test system. Rate capability tests were performed at C/10, C/8, C/5, C/3 and C/2 rates (1C = 1675 mA g_S^{-1}). Cycling tests

were also performed at constant currents of C/5, C/3, and C/2 rates over 100 cycles with a previous activation at a C/20 rate (first cycle). Both specific capacity and current rate are referred to the sulfur mass in the positive electrode.

All the electrochemical tests were performed at room temperature (25 °C).

3. Results and Discussion

Important characteristics allowing the application of a carbon material in lithium sulfur cell are represented by the high surface area, and the presence of a suitable porosity for efficiently hosting sulfur and increasing the electrode conductivity. Fig. 2a shows N_2-adsorption/desorption isotherms of GO and 3DNG, both attributed to the IV type of the BDDT classification. The figure reveals a hysteresis loop typical of mesoporous materials with similar shape for the 3DNG and GO, and a remarkably different surface area and pore volume for the two samples. The estimated surface area and pore volume by BET method are 369 $m^2\ g^{-1}$ and 0.36 $cm^3\ g^{-1}$ for 3DGN, and 56 $m^2\ g^{-1}$ and 0.06 $cm^3\ g^{-1}$ for GO, respectively, thus indicating an increase of the two parameters by more than 6 times due to the microwave-assisted exfoliation and reduction. DFT model has been applied to calculate the pore size distribution of 3DNG as shown in Fig. 2a inset, which reveals three peaks ranging from 1.6 nm to 3.9 nm suggesting an interconnected pore system formed by micro and mesopores, while peaks in the pore size distribution of GO were hardly discernible (data not shown). Such a porous structure of 3DNG is expected to provide suitable sites for hosting sulfur, however minor sulfur amount may be deposited outside the pores as evidenced by literature papers [45,46].

Further information on structure and composition of 3DNG is provided by coupling Raman and X-ray photoelectron spectroscopies (XPS), as well as by elemental analysis, respectively. Fig. 2b reports the comparison of the Raman spectra of bare graphite, GO and 3DNG samples. Graphite spectrum reveals the typical response,

characterized by the G peak at 1590 cm^{-1}, ascribed to the stretching of sp^2 carbon bonds in both rings and chains, 2D peak at ~ 2700 cm^{-1}, and a small D peak attributed to the breathing modes of sp^2 atoms in rings activated by the presence of defects [47,48]. The conversion of graphite in GO and 3DGN gives rise to a significant increase of the D band, reflected by the high ratio between D and G bands (I_D/I_G), which suggests formation of further defects due to the chemical treatment, subsequent exfoliation and reduction processes undergone by graphite [48]. Further differences between GO and 3DNG are observed by the comparison between XPS spectra reported in Fig. 2c. The XPS spectrum of GO shows two peaks, at 284.8 and 530.6 eV, attributed to C1s and O1s, respectively, while the one of 3DNG indicates the presence of a further peak at 399.6 eV attributed to N1s signal, hence confirming the actual inclusion of nitrogen in the carbonaceous material (3DNG) by the adopted synthetic pathway. The C1s peak of GO magnified in Fig. 2d has been fitted by four components centered at 284.8, 286.7, 288.0, and 289.0 eV, which are attributed to the C=C/C–C in aromatic rings, C–O alkoxy/epoxy, C=O, and O–C=O groups, respectively [49], being dominant the C–O signal as expected.

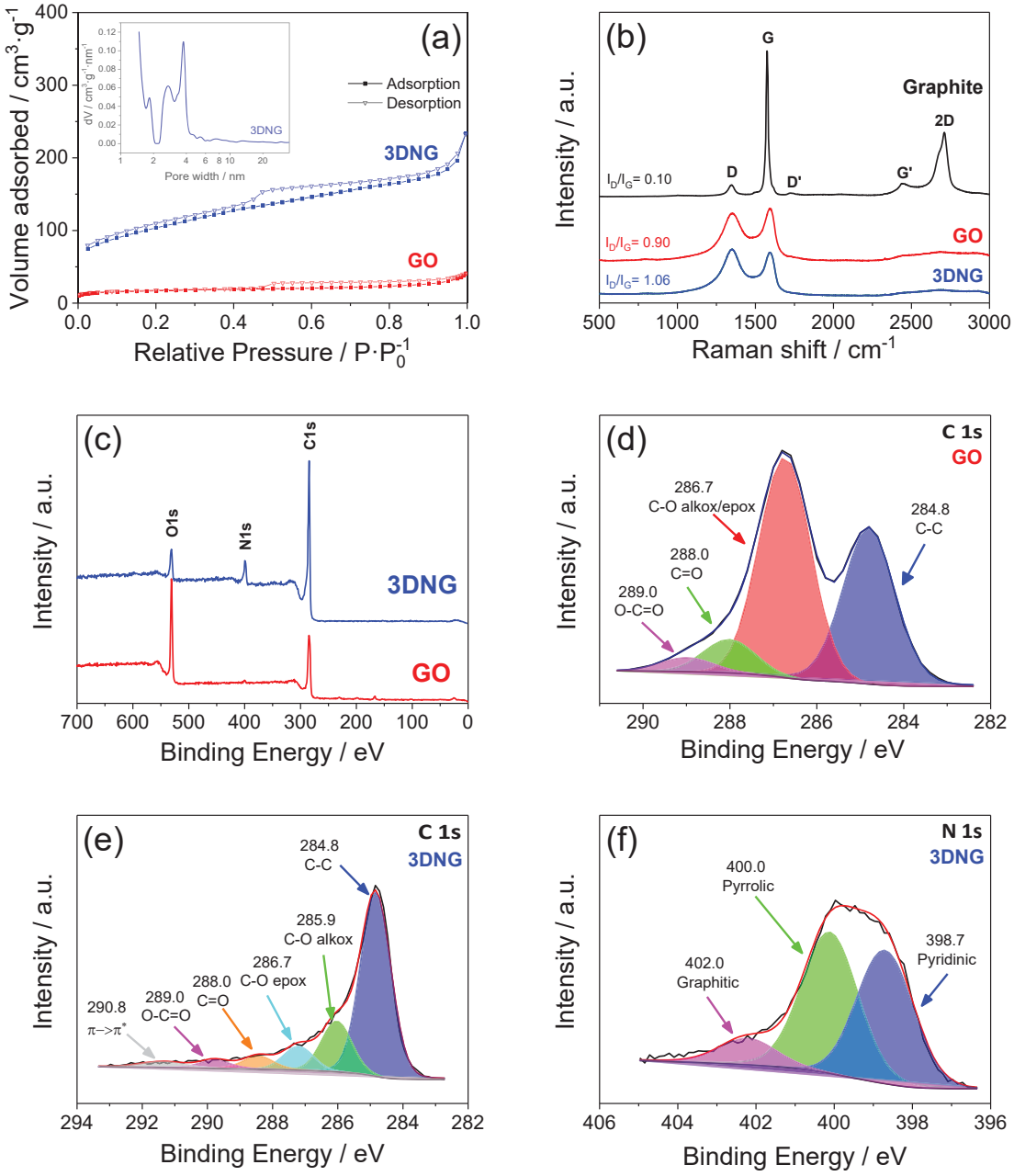

Figure 2. (a) N_2 adsorption/desorption isotherms of GO and 3DNG samples; figure inset: pore size distribution calculated by the DFT model applied to 3DNG. **(b)** Raman spectra of graphite, GO and 3DNG. **(c)** XPS spectra of GO and 3DNG. **(d)** XPS spectra for the C 1s photoemission peak of GO. **(e, f)** XPS for the **(e)** C 1s photoemission peak and **(f)** N 1s photoemission peak of 3DNG sample. See experimental section for samples' acronym.

The 3DNG material shows a rather different C1s spectrum (Fig. 2e), characterized by a strong C=C/C–C contribution with respect to the other components, and by the presence of single alkoxy and epoxy components as well as a very weak peak around

290.8 eV, assigned to a $\pi \rightarrow \pi^*$ transition [50], as reported in Table 1 comparing the percent contribution of the C=C/C–C in aromatic rings, C–O alkoxy/epoxy, C=O and O–C=O groups as well as the $\pi \rightarrow \pi^*$ transition to the C1s photoemission peak of GO and 3DNG. This evidence indicates the remarkable effect on the surface functional groups of the solvothermal treatment, mostly leading to reduction. The N1s spectrum of 3DNG (Fig. 2f) has been fitted by three components with binding energies of 398.7, 400.0 and 402.0 eV, corresponding to pyridinic, pyrrolic and graphitic N, respectively [51]. The first two are the predominant forms, with contribution of 42.99 and 48.06 %, respectively, whereas the graphitic form only represents the 8.96 %.

Sample	C=C/C–C 284.8 eV	C–O alkoxy 285.9 eV	C–O epoxy 286.7 eV	C=O carbonyl 288.0 eV	C–O carboxyl 289.0 eV	$\pi \rightarrow \pi^*$ 290.8 eV
GO	38.12 %	--	50.97 %	7.69 %	3.22 %	--
3DNG	63.21 %	17.43 %	8.14 %	4.95 %	3.13 %	3.14 %

Table 1. Percent contribution of the six components used in the fitting of the C1s photoemission peak of GO and 3DNG samples (see Figure 1b-d and the related discussion).

The presence of functional groups involving pyridinic and pyrrolic nitrogen shown by XPS for the 3DNG sample is considered very advantageous characteristic, suitable for adsorbing lithium polysulfide [52], and enhancing the electrochemical characteristics of Li-S battery. Thus, the herein proposed 3DNG material has been impregnated with sulfur to form a 3-dimensional N-doped graphene-sulfur composite (3DNG-S). Fig. 3a shows the XRD patterns of pristine 3DNG and 3DNG-S composite. The characteristic peak of GO occurring at about 11° (2θ) [53] is absent in the 3DNG pattern, thus suggesting exfoliation and reduction of GO during the solvothermal treatment. The resulting carbon matrix has a partially graphitic character, as revealed by

the broad peak at 26º (2θ) related to the (002) diffraction of graphite, and shows a weaker peak at about 44º (2θ), assigned to either (100) or (101) diffractions in graphene nanosheets [54]. The significant broadening of the peaks indicates a high disorder in the stacking of graphene nanosheets. On the other hand, the 3DNG-S composite exhibits well-defined peaks attributed to the orthorhombic sulfur (PDF # 85-0799), and a small shoulder between 20° and 30º (2θ) related to the 3DNG hosting framework. In particular, TGA suggests a sulfur mass loading in the composite of about 68%, as revealed by a weight loss due to S evaporation observed in the 200-350 ºC range (Fig. 2b, and the related inset showing the differential curve). Actually, the increase of sulfur loading represents a challenging goal for the development of lithium-sulfur cells able to ensure both high energy and relevant power. A recent work reported a similar composite cathode with a sulfur loading of 60 wt.%, leading to a maximum S content of 4.0 mg cm^{-2} over the electrode geometric surface [55]. Furthermore, sulfur loading of 60 and 66 wt.% have been achieved using activated ordered mesoporous carbon and flower-like 3D carbon matrixes, respectively [15,36], while a reasonable S content of 4.0 mg cm^{-2} and good performance have been recently reported for a carbon nanotube-sulfur electrode containing 60 wt.% of sulfur [38]. On the other hand, further increase of the sulfur loading and the energy density may be possibly achieved by limiting negative effects on the electrode conductivity and cell polarization, as well as by adopting new strategies, such as the use of polysulfide containing electrolyte solutions [32].

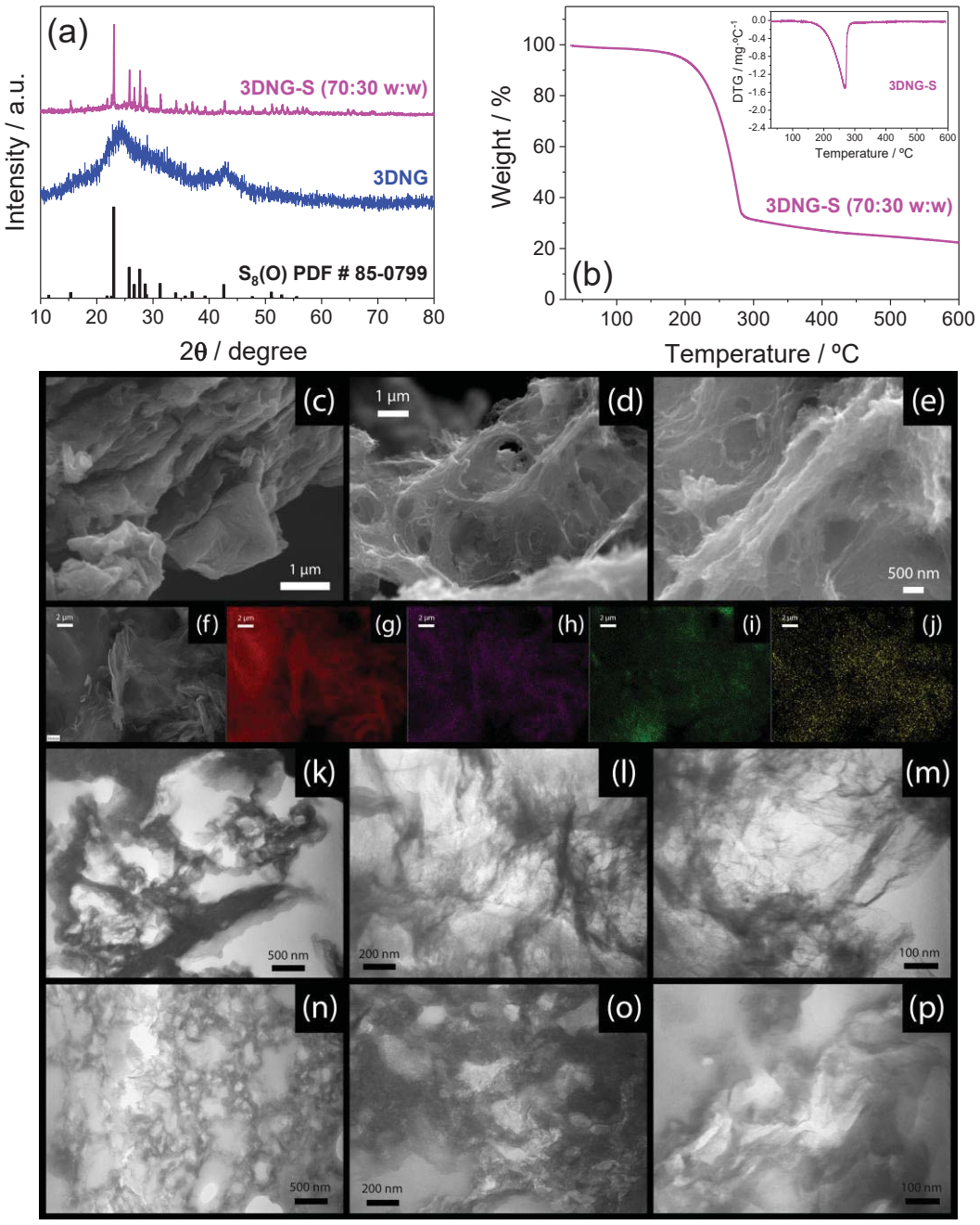

Figure 3. (a) XRD patterns of the 3DNG and 3DNG-S samples; reference data sheet of crystalline S (PDF # 85-0799). **(b)** TGA trace of 3DNG-S composite under a N_2 flow upon heating at 5 ºC min^{-1}; DTG curve in figure inset. **(c-l)** Electron microscopy analysis of the samples. In detail: **(c-e)** SEM images of **(c)** GO and **(d, e)** 3DNG; **(f)** SEM image and **(g-l)** related SEM-EDS elemental maps of **(g)** C, **(h)** O, **(i)** S and **(j)** N for the 3DNG-S composite; **(k-p)** TEM images at several magnifications of **(k-m)** 3DNG and **(n-p)** 3DNG-S. See experimental section for samples' acronym.

The morphology of GO, 3DNG and 3DNG-S was examined by SEM (Fig. 3c-f). The smooth and thick flakes of pristine GO (Fig. 3c) turn into randomly crumpled sheets (Fig. 3 d, e) due exfoliation and layer assembly induced by the solvothermal process. Furthermore, panels f-j of Fig. 3 reveal a homogeneous distribution of C, O, S, and N over the disordered graphene array of 3DNG-S, as suggested by comparison of SEM image (panel f) and EDS maps (panels g-j). The TEM images at several magnifications, reported in panels k-p of Fig. 3, clearly show the remarkably different morphology of 3DNG (panels k-m) and 3DNG-S (panels n-p). Indeed, the single graphene sheets arranged into a 3D network in 3DNG (see panels k-m) are homogenously covered and infiltrated by sulfur to form a smooth agglomerate in 3DNG-S (see panels n-p). Such an interconnected network is expected to ensure an efficient electron and ion transport through the composite, thereby leading to fast electrode charge transfer [25].

As above mentioned, literature works have demonstrated that nitrogen-doping can decrease the polysulfides dissolution into the electrolyte [4], thus improving the cathode performance. However, such an optimized material may be not sufficient for achieving high performances in a lithium sulfur cell which requires a suitable electrolyte, leading to the formation of a stable and uniform SEI on the lithium-metal electrode, and preventing the possible polysulfide shuttle [4]. Solutions of lithium salt (e.g., LiTFSI) in DOL and DME solvents, added by $LiNO_3$ as the film forming agent, have been widely proposed and studied in literature as the most suitable electrolyte media for Li/S cell. However, the volatility of these solvents causes relevant flammability of the electrolyte, thus posing some safety concern [56]. Therefore, we have selected and studied herein an alternative, diglyme-based electrolyte, namely DEGDME-LiTFSI-$LiNO_3$ [38], which has suitable electrochemical features for application in Li/S, such as comparable conductivity and interface resistance with respect to DOL:DME-LiTFSI-$LiNO_3$, while a relevantly lower flammability as will be demonstrated hereafter. The composition in terms of chemical

nature of the species and lithium salt concentration may mat actually affect the electrolyte characteristics and the cell performances. Accordingly, the LiTFSI concentration in ether-based solutions may affect the electrolyte decomposition pathways over the anode surface upon SEI formation and alter the Li^+ solvation shell, with possible effects on the cell behavior [57]. In particular, high LiTFSI concentration and $LiNO_3$ addition may weaken the Li^+-solvent interactions [58]. Furthermore, the increase of salt concentration is expected to decrease the electrolyte flammability, although it may raise the viscosity and possibly lower the conductivity [59]. Herein, we have proposed DEGDME dissolving 1 mol kg^{-1} of LiTFSI and 1 mol kg^{-1} of $LiNO_3$ as electrolyte solution favorably combining high conductivity, moderate flammability, and suitable electrode interface.

Fig. 4 reports the EIS Nyquist plots detected at room temperature for determining the conductivity (panel a) and the interface resistance (panel b), as well as the flammability (panels c-f) of DEGDME-LiTFSI-$LiNO_3$ electrolyte and DOL:DME-LiTFSI-$LiNO_3$ reference solution. The Nyquist plots of the two electrolytes in symmetrical blocking electrode cells reported in Fig. 4a show slightly higher resistance of the diglyme-based electrolyte with respect to the reference (see corresponding equivalent circuit in inset), thus lower value of the conductivity which is calculated to be of 4.6 × 10^{-3} S cm^{-1} and 7.9× 10^{-3} S cm^{-1}, respectively. Furthermore, the impedance responses in symmetrical Li/Li cells reported in Fig. 4b suggest a suitable, lowly resistive Li/electrolyte interface for both electrolytes, characterized by high-frequency and a middle frequency semi-circles, which have been analyzed by NLLS fit [60] using the equivalent circuit shown in Fig. 4b inset. Despite the significant role of the electrolyte composition in determining the EIS response, we may reasonably attribute the high-frequency semicircle to the SEI at the electrode surface [61], while the middle-low-frequency spectrum either to charge transfer or to diffusion processes [62], mostly depending on the frequency. Accordingly, considering the semicircles with frequency

ranging from 500 kHz to about 100 Hz we have calculated SEI resistance values (R_{i1}) of 86 ± 2 Ω and 62 ± 2 Ω for DEGDME-LiTFSI-$LiNO_3$ and DOL:DME-LiTFSI-$LiNO_3$, respectively. Furthermore, semicircles with frequency ranging from about 100 Hz to 1 Hz were attributed to the charge transfer process at the electrode/electrolyte interphase, with resistance of values (R_{i2}) of 100 ± 10 Ω and 71 ± 7 Ω for DEGDME-LiTFSI-$LiNO_3$ and DOL:DME-LiTFSI-$LiNO_3$, respectively. Flammability tests have been carried out on both electrolytes (Fig. 4c-f), by exposing the samples to a butane flame. Fig. 4c reveals that DOL:DME-LiTFSI-$LiNO_3$ directly ignites by exposure to flame with an immediate fire evolution, while DEGDME-LiTFSI-$LiNO_3$ does not show any sign of fire under the same condition (Fig. 4d). The absence of fire evolution and direct ignition of the diglyme-based electrolyte was already observed by our group in a previous work and confirmed herein by adopting the same experimental setup [38]. In this work we have further increased the exposure time to check electrolyte ignition limit which is determined by its vapor pressure within the adopted condition. Accordingly, Fig. 4e shows the absence of fire evolution by exposure of the DEGDME-LiTFSI-$LiNO_3$ electrolyte to flame prolonged to 10 s, while only after 15 s of exposure the electrolyte reveals fire evolution with a red-pink flame related to the optical emission of Li^+, thus suggesting the evaporation of the solvent (Fig. 4f). The relevant stability and low flammability of the DEGDME-LiTFSI-$LiNO_3$ as well as its high conductivity and low interface resistance suggest its full applicability in Li/S battery.

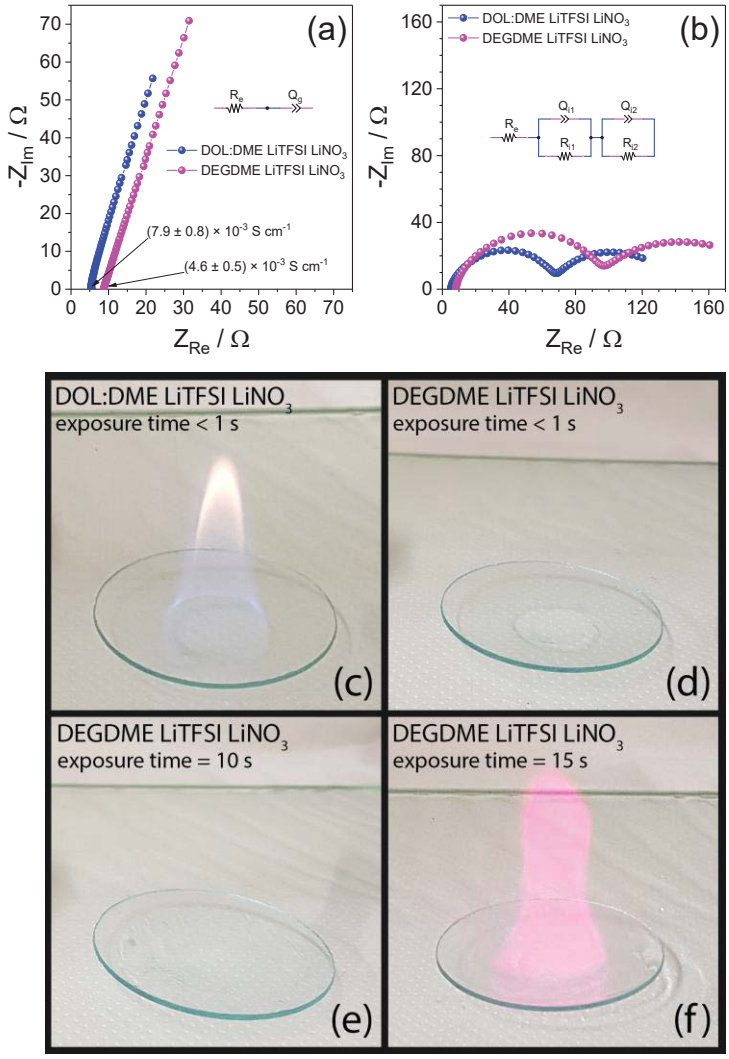

Figure 4. (a, b) Impedance spectra of symmetrical **(a)** SS/SS and **(b)** Li/Li cells using DEGDME-LiTFSI-$LiNO_3$ electrolyte and DOL:DME-LiTFSI-$LiNO_3$ reference solution; equivalent circuits used for NLLS fit [60] of the spectra are reported in inset; ionic conductivities are calculated by taking the EIS responses of panel **a** (see the experimental for further details). **(c-f)** Flammability tests of **(c)** DOL:DME-LiTFSI-$LiNO_3$ reference and **(d-f)** DEGDME-LiTFSI-$LiNO_3$ electrolyte through direct exposure to a butane flame. In detail: **(c)** flame evolution in DOL:DME-LiTFSI-$LiNO_3$ after exposure time < 1 s (direct ignition); **(d, e)** absence of flame in DEGDME-LiTFSI-$LiNO_3$ after **(d)** exposure time < 1s and **(e)** exposure time = 10 s; **(f)** flame evolution in DEGDME-LiTFSI-$LiNO_3$ after exposure time = 15 s. See experimental section for samples' acronym.

The 3DNG-S composite cathode has been therefore studied in the DEGDME-LiTFSI-$LiNO_3$ electrolyte by CV, as reported in Fig. 5a. The figure reveals two reduction peaks occurring at about 2.4 V and 1.9 V upon the first reduction scan, associated with the S conversion to long-chain (Li_2S_x, $6 \leq x \leq 8$) and short-chain Li_2S_2/Li_2S (Li_2S_x, $1 \leq x \leq 4$) lithium polysulfides, respectively [38,55]. Upon the subsequent oxidation, a broad signal consisting of two overlapping peaks of different intensity occurs from 2.2 V to 2.6 V. The current peaks are positioned at 2.4 V and at 2.5 V, respectively, and are attributed to the conversion of lithium sulfide to soluble lithium polysulfides and to sulfur [63]. During subsequent cycles the potential of the oxidation peaks hardly varies, while that of the cathodic peaks shift to a higher value, that is, 2.43 V and 1.95 V, with consequent decrease of the cell polarization, thus suggesting a well reversible process and the formation of a stable and lowly-resistive interphase [38,55]. The decreasing trend of the electrode/electrolyte interphase resistances upon cycling is confirmed by EIS measurements recorded at the OCV, after 6 and 12 voltammetry cycles. The related Nyquist plots (Fig. 5 b-d), have been analyzed by NLLS method [60] using the equivalent circuits reported in figure insets. The spectra reveal the contribution of various cell features reflected into sub-circuits arranged in series, i.e., the high-frequency ohmic electrolyte resistance (R_e), parallel arrays of high-middle-frequency interphase resistances ($R_{i,n}$, with n = 1, 2, 3) and pseudo-capacitances ($Q_{i,n}$ with n = 1, 2, 3), and a low-frequency pseudo-capacitance accounting for either semi-infinite Li^+ diffusion or capacitive behavior of the cell [64–66]. Table 2 reports the interphase resistance values calculated by NLLS fit [60] and the related χ^2, which is below 1×10^{-3} for all the analyses. Moreover, panels b, c, and d of Fig. 5 indicate good agreement between simulated and experimental data, thus further confirming the accuracy of the NLLS analysis. The modeled sub-circuits reflect the contribution of both anode and cathode sides due to the two-electrode cell configuration adopted for the study, thereby providing

useful information about the electrochemical stability of the DEGDME-LiTFSI-$LiNO_3$ electrolyte towards lithium metal and 3DNG-S electrode. Accordingly, EIS reveals a significant decrease of the overall electrode/electrolyte interphase resistances upon cycling, from about 55 ± 4 Ω at the OCV to 6.6 ± 0.2 Ω after 6 cycles; then, the resistance slightly increases to 16.4 ± 0.8 Ω after 12 cycles (corresponding CV profiles not shown).

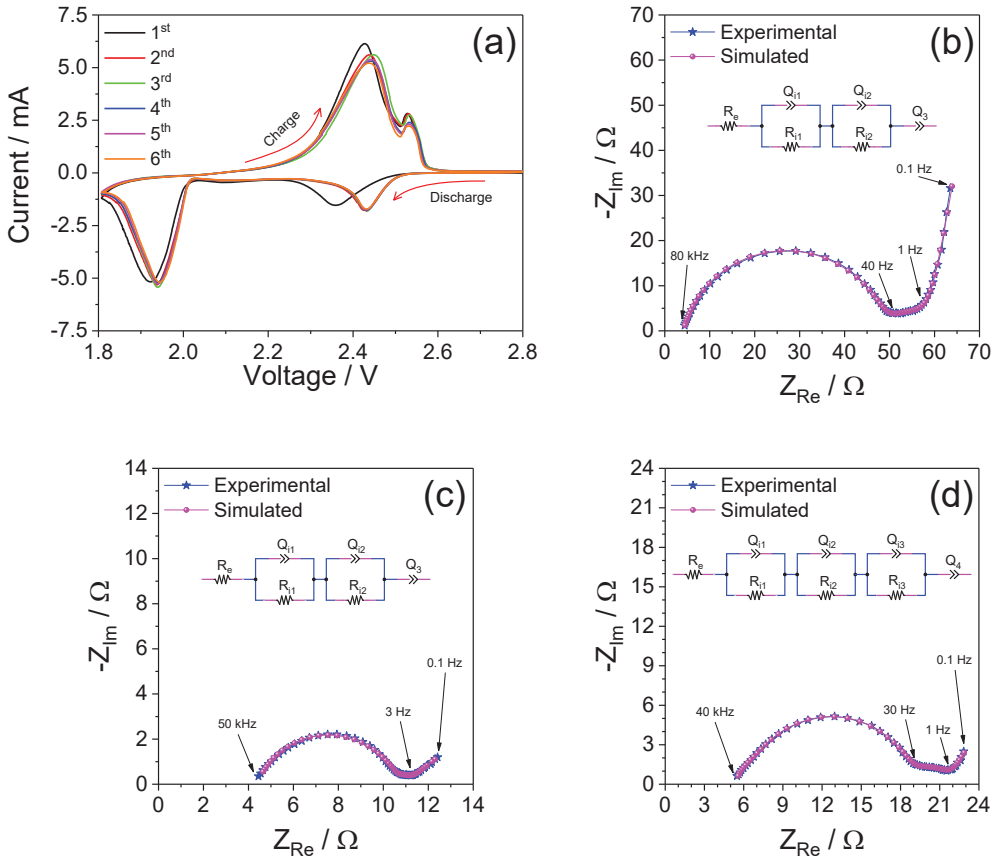

Figure 5. (a) Cyclic voltammetry of Li/DEGDME-LiTFSI-$LiNO_3$/3DNG-S cell at a scan rate of 0.1 mV s^{-1}. **(b-d)** Impedance spectra of the cell **(b)** at the OCV, **(c)** after 6 and **(d)** after 12 voltammetry cycles; equivalent circuits used for NLLS fit [60] of the spectra are reported in inset. See experimental section for samples' acronym.

The remarkable decrease of the cell impedance well justifies the decrease of the cell polarization observed by CV, and suggest a pre-cycling of the cell as suitable activation step for achieving high performances [38]. Furthermore, the low electrode/electrolyte impedance observed by the EIS tests, the complete overlapping of

CV profiles after the first cycle, and the absence of relevant decay indicate for the Li/DEGDME-LiTFSI-$LiNO_3$/3DNG-S cell a reversible process with enhanced stability and fast charge transfer. As above mentioned, these optimized electrochemical characteristics are herein attributed to the enhanced structure and morphology of 3DNG-S electrode, as well as to suitably high conductivity and film forming ability of the electrolyte.

Cell condition	**Circuit**	**R_{i1} / Ω**	**R_{i2} / Ω**	**R_{i3} / Ω**	**χ^2**
OCV	$R_e(R_{i,1}Q_{i,1})(R_{i,2}Q_{i,2})Q_3$	44.9 ± 1.0	10 ± 3	-	4.7×10^{-4}
After 6 cycles	$R_e(R_{i,1}Q_{i,1})(R_{i,2}Q_{i,2})Q_3$	6.29 ± 0.06	0.27 ± 0.14	-	4.6×10^{-5}
After 12 cycles	$R_e(R_{i,1}Q_{i,1})(R_{i,2}Q_{i,2})(R_{i,3}Q_{i,3})Q_3$	1.1 ± 0.2	12.4 ± 0.3	2.9 ± 0.3	1.6×10^{-5}

Table 2. Results of NLLS analyses [60] performed on the impedance spectra of Fig. 4b-c, recorded upon cyclic voltammetry of the Li/DEGDME-LiTFSI-$LiNO_3$/3DNG-S cell at the OCV, after 6 and after 12 cycles. In detail: employed equivalent circuit, interphase resistance and χ^2 value of the fit. See experimental section for samples' acronym.

The Li/DEGDME-LiTFSI-$LiNO_3$/3DNG-S cell is then studied by galvanostatic cycling at several operating currents, with the aim of evaluating the suitability of the system for energy storage. The rate capability test, performed with currents ranging from C/10 to C/2, is reported in Fig. 6 in terms of voltage profiles (panel a) and cycling trend (panel b). The cell voltage evolves by the two plateaus expected for the Li/S conversion process during galvanostatic charge and discharge, as already observed by CV tests (compare Fig. 6a with Fig. 5a), with relatively low cell polarization increasing from 0.15 V at C/10 to 0.26 V at C/2. Furthermore, the cycling response of Fig. 6b shows that the cell delivers a reversible capacity of about 1400, 1300, 1190, 1100 and 1050 mAh g_S^{-1} at

current rates of C/10, C/8, C/5, C/3, and C/2, and recovers a discharge capacity of about 1300 mAh g_S^{-1} when the C-rate is lowered back to C/10 after the 25th cycle.

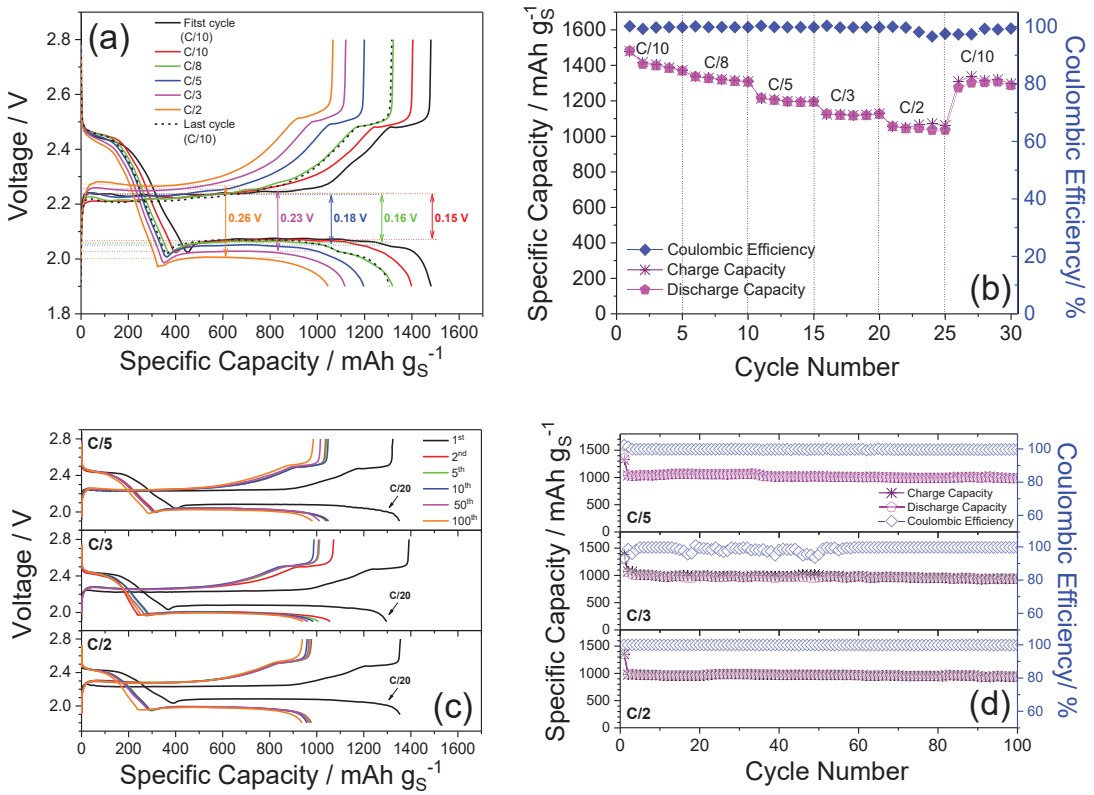

Figure 6. (a, b) Rate capability test in terms of **(a)** voltage profile and **(b)** galvanostatic cycling behavior performed at C/10, C/8, C/5, C/3 and C/2 rates of the Li/DEGDME-LiTFSI-$LiNO_3$/3DNG-S cell. **(c, d)** Galvanostatic tests at C/5, C/3 and C/2 in terms of **(c)** voltage profiles and **(d)** cycling behavior. Voltage range: 1.9 – 2.8 V. 1C = 1675 mA g_S^{-1}. See experimental section for samples' acronym.

The Li/DEGDME-LiTFSI-$LiNO_3$/3DNG-S cell has been studied by prolonged cycling at constant currents of C/5, C/3 and C/2 (Fig. 6c, d) after a first-cycle activation cycle performed at C/20. Fig. 6c shows the voltage profiles of the 1st, 2nd, 5th, 10th, 50th and 100th cycles of the cells, while Fig. 6d reports the corresponding cycling trend. The cells exhibit discharge capacity of about 1050 mAh g_S^{-1} at C/5 and C/3 rates, and 977 mAh g_S^{-1} at C/2, a relevant retention of the voltage profile (Fig. 6c), and a Coulombic

efficiency approaching 100% (Fig. 6d). After 100 cycles all the cells remarkably evidence a capacity retention higher that 95%, which well confirms the enhanced electrode electrolyte interphase above discussed.

Conclusions

A nitrogen-doped carbon material consisting of three-dimensional graphene array (3DNG) was prepared by simple microwave-assisted solvothermal pathway and used for homogeneously hosting crystalline sulfur and achieving a composite cathode (3DNG-S) suitable for application in high performance lithium battery. Raman, XPS, TGA, SEM and TEM analyses indicated a cathode formed by a N-functionalized carbon matrix with low graphitic character and micro- and mesoporosity, which hosts large amount of crystalline sulfur, i.e., the 68 wt.% of the composite. The resulting 3DNG-S composite was studied in lithium-metal cell with the DEGDME-LiTFSI-$LiNO_3$ electrolyte solution. The diglyme electrolyte showed high conductivity (above 10^{-3} S cm^{-1}) and suitable electrode/electrolyte interface, revealed by electrochemical impedance spectroscopy, as well as remarkably low flammability compared to a reference electrolyte based on DOL and DME solvents. The complete overlapping of the voltammetry profiles and the low electrode/electrolyte impedance observed during CV tests suggested for the Li/DEGDME-LiTFSI-$LiNO_3$/3DNG-S cell a reversible process with enhanced stability and fast charge transfer upon charge and discharge. The Li/DEGDME-LiTFSI-$LiNO_3$/3DNG-S cell exhibited a very stable specific capacity of about 1000 mAh g_S^{-1} with Coulombic efficiency approaching 100% within the C/5 – C/2 current range, a capacity retention higher than 95%, and an excellent rate capability with maximum capacity of 1400 mAh g_S^{-1}. Such an electrochemical performance, which is characteristic of batteries based on N-doped graphene synthesized from GO [67–77], is enhanced in this work by further improving the electrode structure and morphology as well as by

adopting the DEGDME-LiTFSI-$LiNO_3$ electrolyte. Accordingly, the calculated energy density for the Li/DEGDME-LiTFSI-$LiNO_3$/3DNG-S battery approaches to 3000 Wh kg^{-1} with respect to the sulfur mass, which may lead to a practical energy density at C/2 rate of about 700 Wh kg^{-1}, estimated considering a correction factor of 1/3 that takes into account the contribution of anode, electrolyte and inactive components of typical cells [78]. These performances are considered well suitable for high and efficient energy-storage applications.

Acknowledgements

This work was performed with the financial support of the Ministerio de Economía y Competitividad (Project MAT2014-59907-R and MAT2017-87541-R) and Junta de Andalucía (Group FQM-175). The work was carried out within the collaboration project "Accordo di Collaborazione Quadro 2015" between the University of Ferrara (Department of Chemical and Pharmaceutical Sciences) and the Sapienza University of Rome (Department of Chemistry), and founded by the grant "Fondo di Ateneo per la Ricerca Locale (FAR) 2017". The authors thank Dr. Daniela Palmeri of the Electron Microscopy Centre, Department of Chemical and Pharmaceutical Sciences, University of Ferrara, for performing SEM and TEM.

References

[1] D. Larcher, J.-M. Tarascon, Towards greener and more sustainable batteries for electrical energy storage, U.S. Geological Survey, Nat. Chem. 7 (2014) 19–29. doi:10.1038/nchem.2085.

[2] P. Poizot, F. Dolhem, Clean energy new deal for a sustainable world: from non-CO_2 generating energy sources to greener electrochemical storage devices, Energy Environ. Sci. 4 (2011) 2003. doi:10.1039/c0ee00731e.

[3] D. Di Lecce, R. Verrelli, J. Hassoun, Lithium-ion batteries for sustainable energy storage: recent advances towards new cell configurations, Green Chem. 19 (2017) 3442–3467. doi:10.1039/C7GC01328K.

[4] L. Carbone, S.G. Greenbaum, J. Hassoun, Lithium sulfur and lithium oxygen batteries: new frontiers of sustainable energy storage, Sustain. Energy Fuels. 1 (2017) 228–247. doi:10.1039/C6SE00124F.

[5] P.G. Bruce, S.A. Freunberger, L.J. Hardwick, J.-M. Tarascon, Li–O_2 and Li–S batteries with high energy storage, Nat. Mater. 11 (2012) 19–29. doi:10.1038/nmat3191.

[6] Y. Yang, G. Zheng, Y. Cui, Nanostructured sulfur cathodes, Chem. Soc. Rev. 42 (2013) 3018. doi:10.1039/c2cs35256g.

[7] B. Scrosati, J. Garche, Lithium batteries: Status, prospects and future, J. Power Sources. 195 (2010) 2419–2430. doi:10.1016/j.jpowsour.2009.11.048.

[8] A. Manthiram, Y. Fu, S. Chung, C. Zu, Y. Su, Rechargeable Lithium–Sulfur Batteries, Chem. Rev. 114 (2014) 11751–11787. doi:10.1021/cr500062v.

[9] R. Fang, S. Zhao, Z. Sun, D.-W. Wang, H.-M. Cheng, F. Li, More Reliable Lithium-Sulfur Batteries: Status, Solutions and Prospects, Adv. Mater. 29 (2017) 1606823. doi:10.1002/adma.201606823.

[10] C. Zhang, H. Bin Wu, C. Yuan, Z. Guo, X.W. Lou, Confining sulfur in double-shelled hollow carbon spheres for lithium-sulfur batteries, Angew. Chemie - Int. Ed. 51 (2012) 9592–9595. doi:10.1002/anie.201205292.

[11] J. Hassoun, M. Agostini, A. Latini, S. Panero, Y.-K. Sun, B. Scrosati, Nickel-Layer Protected, Carbon-Coated Sulfur Electrode for Lithium Battery, J. Electrochem. Soc. 159 (2012) A390. doi:10.1149/2.039204jes.

[12] J. Kim, D.J. Lee, H.G. Jung, Y.K. Sun, J. Hassoun, B. Scrosati, An advanced lithium-sulfur battery, Adv. Funct. Mater. 23 (2013) 1076–1080. doi:10.1002/adfm.201200689.

[13] M. Agostini, J. Hassoun, A lithium-ion sulfur battery using a polymer, polysulfide-added membrane, Sci. Rep. 5 (2015) 7591. doi:10.1038/srep07591.

[14] L. Carbone, J. Peng, M. Agostini, M. Gobet, M. Devany, B. Scrosati, S. Greenbaum, J. Hassoun, Carbon Composites for a High-Energy Lithium-Sulfur Battey with a Glyme-Based Electrolyte, ChemElectroChem. 4 (2017) 209–215. doi:10.1002/celc.201600586.

[15] N. Moreno, A. Caballero, J. Morales, M. Agostini, J. Hassoun, Lithium battery using sulfur infiltrated in three-dimensional flower-like hierarchical porous carbon electrode, Mater. Chem. Phys. 180 (2016) 82–88. doi:10.1016/j.matchemphys.2016.05.044.

[16] J. Guo, J. Zhang, F. Jiang, S. Zhao, Q. Su, G. Du, Microporous carbon nanosheets derived from corncobs for lithium–sulfur batteries, Electrochim. Acta. 176 (2015) 853–860. doi:10.1016/j.electacta.2015.07.077.

[17] N. Moreno, A. Caballero, L. Hernán, J. Morales, J. Canales-Vázquez, Ordered mesoporous carbons obtained by a simple soft template method as sulfur immobilizers for lithium–sulfur cells, Phys. Chem. Chem. Phys. 16 (2014) 17332–17340. doi:10.1039/C4CP02829E.

[18] H. Kim, H.-D. Lim, J. Kim, K. Kang, Graphene for advanced Li/S and Li/air batteries, J. Mater. Chem. A. 2 (2014) 33–47. doi:10.1039/C3TA12522J.

[19] X. Yang, L. Zhang, F. Zhang, Y. Huang, Y. Chen, Sulfur-Infiltrated Graphene-Based Layered Porous Carbon Cathodes for High-Performance Lithium–Sulfur

Batteries, ACS Nano. 8 (2014) 5208–5215. doi:10.1021/nn501284q.

[20] H.M. Kim, H.-H. Sun, I. Belharouak, A. Manthiram, Y.-K. Sun, An Alternative Approach to Enhance the Performance of High Sulfur-Loading Electrodes for Li–S Batteries, ACS Energy Lett. 1 (2016) 136–141. doi:10.1021/acsenergylett.6b00104.

[21] M. Li, Y. Wan, J.K. Huang, A.H. Assen, C.E. Hsiung, H. Jiang, Y. Han, M. Eddaoudi, Z. Lai, J. Ming, L.J. Li, Metal-Organic Framework-Based Separators for Enhancing Li-S Battery Stability: Mechanism of Mitigating Polysulfide Diffusion, ACS Energy Lett. 2 (2017) 2362–2367. doi:10.1021/acsenergylett.7b00692.

[22] J. Ming, M. Li, P. Kumar, L.J. Li, Multilayer Approach for Advanced Hybrid Lithium Battery, ACS Nano. 10 (2016) 6037–6044. doi:10.1021/acsnano.6b01626.

[23] W. Wahyudi, Z. Cao, P. Kumar, M. Li, Y. Wu, M.N. Hedhili, T.D. Anthopoulos, L. Cavallo, L. Li, J. Ming, Phase Inversion Strategy to Flexible Freestanding Electrode : Critical Coupling of Binders and Electrolytes for High Performance Li – S Battery, 1802244 (2018) 1–8. doi:10.1002/adfm.201802244.

[24] H. Gao, H. Duan, 2D and 3D graphene materials: Preparation and bioelectrochemical applications, Biosens. Bioelectron. 65 (2015) 404–419. doi:10.1016/j.bios.2014.10.067.

[25] S. Lu, Y. Chen, X. Wu, Z. Wang, Y. Li, Three-Dimensional Sulfur/Graphene Multifunctional Hybrid Sponges for Lithium-Sulfur Batteries with Large Areal Mass Loading, Sci. Rep. 4 (2015) 4629. doi:10.1038/srep04629.

[26] G. Zhou, L. Li, C. Ma, S. Wang, Y. Shi, N. Koratkar, W. Ren, F. Li, H.-M. Cheng, A graphene foam electrode with high sulfur loading for flexible and high energy

Li-S batteries, Nano Energy. 11 (2015) 356–365. doi:10.1016/j.nanoen.2014.11.025.

[27] A. Schneider, J. Janek, T. Brezesinski, Improving the capacity of lithium–sulfur batteries by tailoring the polysulfide adsorption efficiency of hierarchical oxygen/nitrogen-functionalized carbon host materials, Phys. Chem. Chem. Phys. 19 (2017) 8349–8355. doi:10.1039/C6CP08865A.

[28] J. Song, M.L. Gordin, T. Xu, S. Chen, Z. Yu, H. Sohn, J. Lu, Y. Ren, Y. Duan, D. Wang, Strong Lithium Polysulfide Chemisorption on Electroactive Sites of Nitrogen-Doped Carbon Composites For High-Performance Lithium-Sulfur Battery Cathodes, Angew. Chemie Int. Ed. 54 (2015) 4325–4329. doi:10.1002/anie.201411109.

[29] T. Van Khai, H.G. Na, D.S. Kwak, Y.J. Kwon, H. Ham, K.B. Shim, H.W. Kim, Significant enhancement of blue emission and electrical conductivity of N-doped graphene, J. Mater. Chem. 22 (2012) 17992. doi:10.1039/c2jm33194b.

[30] S. Zhang, K. Ueno, K. Dokko, M. Watanabe, Recent Advances in Electrolytes for Lithium-Sulfur Batteries, Adv. Energy Mater. 5 (2015) 1500117. doi:10.1002/aenm.201500117.

[31] M. Agostini, D.-J. Lee, B. Scrosati, Y.K. Sun, J. Hassoun, Characteristics of Li2S8-tetraglyme catholyte in a semi-liquid lithium–sulfur battery, J. Power Sources. 265 (2014) 14–19. doi:10.1016/j.jpowsour.2014.04.074.

[32] S.-K.K. Lee, S.-M.M. Oh, E. Park, B. Scrosati, J. Hassoun, M.-S.S. Park, Y.-J.J. Kim, H. Kim, I. Belharouak, Y.-K.K. Sun, Highly Cyclable Lithium–Sulfur Batteries with a Dual-Type Sulfur Cathode and a Lithiated Si/SiO x Nanosphere Anode, Nano Lett. 15 (2015) 2863–2868. doi:10.1021/nl504460s.

[33] M. Agostini, B. Scrosati, J. Hassoun, An Advanced Lithium-Ion Sulfur Battery for High Energy Storage, Adv. Energy Mater. 5 (2015) 1500481. doi:10.1002/aenm.201500481.

[34] S.-H. Chung, C.-H. Chang, A. Manthiram, A core–shell electrode for dynamically and statically stable Li–S battery chemistry, Energy Environ. Sci. 9 (2016) 3188–3200. doi:10.1039/C6EE01280A.

[35] L. Carbone, M. Gobet, J. Peng, M. Devany, B. Scrosati, S. Greenbaum, J. Hassoun, Comparative Study of Ether-Based Electrolytes for Application in Lithium-Sulfur Battery, ACS Appl. Mater. Interfaces. 7 (2015) 13859–13865. doi:10.1021/acsami.5b02160.

[36] N. Moreno, M. Agostini, A. Caballero, J. Morales, J. Hassoun, A long-life lithium ion sulfur battery exploiting high performance electrodes, Chem. Commun. 51 (2015) 14540–14542. doi:10.1039/C5CC05162B.

[37] W. Li, H. Yao, K. Yan, G. Zheng, Z. Liang, Y.-M. Chiang, Y. Cui, The synergetic effect of lithium polysulfide and lithium nitrate to prevent lithium dendrite growth, Nat. Commun. 6 (2015) 7436. doi:10.1038/ncomms8436.

[38] L. Carbone, T. Coneglian, M. Gobet, S. Munoz, M. Devany, S. Greenbaum, J. Hassoun, A simple approach for making a viable, safe, and high-performances lithium-sulfur battery, J. Power Sources. 377 (2018) 26–35. doi:10.1016/j.jpowsour.2017.11.079.

[39] H. Chen, C. Wang, W. Dong, W. Lu, Z. Du, L. Chen, Monodispersed Sulfur Nanoparticles for Lithium–Sulfur Batteries with Theoretical Performance, Nano Lett. 15 (2015) 798–802. doi:10.1021/nl504963e.

[40] C. Wang, H. Chen, W. Dong, J. Ge, W. Lu, X. Wu, L. Guo, L. Chen, Sulfur–amine

chemistry-based synthesis of multi-walled carbon nanotube–sulfur composites for high performance Li–S batteries, Chem. Commun. 50 (2014) 1202–1204. doi:10.1039/C3CC47223J.

[41] W.S. Hummers, R.E. Offeman, Preparation of Graphitic Oxide, J. Am. Chem. Soc. 80 (1958) 1339–1339. doi:10.1021/ja01539a017.

[42] G. Zhou, E. Paek, G.S. Hwang, A. Manthiram, Long-life Li/polysulphide batteries with high sulphur loading enabled by lightweight three-dimensional nitrogen/sulphur-codoped graphene sponge, Nat. Commun. 6 (2015) 7760. doi:10.1038/ncomms8760.

[43] F.S. Al-Hazmi, G.H. Al-Harbi, G.W. Beall, A.A. Al-Ghamdi, A.Y. Obaid, W.E. Mahmoud, One pot synthesis of graphene based on microwave assisted solvothermal technique, Synth. Met. 200 (2015) 54–57. doi:10.1016/j.synthmet.2014.12.028.

[44] H.D. Shin, M. Agostini, I. Belharouak, J. Hassoun, Y.-K.K. Sun, High-power lithium polysulfide-carbon battery, Carbon N. Y. 96 (2016) 125–130. doi:10.1016/j.carbon.2015.09.034.

[45] R. Chen, T. Zhao, J. Lu, F. Wu, L. Li, J. Chen, G. Tan, Y. Ye, K. Amine, Graphene-Based Three-Dimensional Hierarchical Sandwich-type Architecture for High-Performance Li/S Batteries, Nano Lett. 13 (2013) 4642–4649. doi:10.1021/nl4016683.

[46] N. Moreno, A. Caballero, L. Hernán, J. Morales, Lithium–sulfur batteries with activated carbons derived from olive stones, Carbon N. Y. 70 (2014) 241–248. doi:10.1016/j.carbon.2014.01.002.

[47] A.C. Ferrari, J.C. Meyer, V. Scardaci, C. Casiraghi, M. Lazzeri, F. Mauri, S.

Piscanec, D. Jiang, K.S. Novoselov, S. Roth, A.K. Geim, Raman Spectrum of Graphene and Graphene Layers, Phys. Rev. Lett. 97 (2006) 187401. doi:10.1103/PhysRevLett.97.187401.

[48] A.C. Ferrari, Raman spectroscopy of graphene and graphite: Disorder, electron–phonon coupling, doping and nonadiabatic effects, Solid State Commun. 143 (2007) 47–57. doi:10.1016/j.ssc.2007.03.052.

[49] A. Abouimrane, O.C. Compton, K. Amine, S.T. Nguyen, Non-Annealed Graphene Paper as a Binder-Free Anode for Lithium-Ion Batteries, J. Phys. Chem. C. 114 (2010) 12800–12804. doi:10.1021/jp103704y.

[50] A. Ganguly, S. Sharma, P. Papakonstantinou, J. Hamilton, Probing the Thermal Deoxygenation of Graphene Oxide Using High-Resolution In Situ X-ray-Based Spectroscopies, J. Phys. Chem. C. 115 (2011) 17009–17019. doi:10.1021/jp203741y.

[51] H. Wang, Y. Wang, Y. Li, Y. Wan, Q. Duan, Exceptional electrochemical performance of nitrogen-doped porous carbon for lithium storage, Carbon 82 (2015) 116–123. doi:10.1016/j.carbon.2014.10.041.

[52] K. Han, J. Shen, S. Hao, H. Ye, C. Wolverton, M.C. Kung, H.H. Kung, Free-Standing Nitrogen-doped Graphene Paper as Electrodes for High-Performance Lithium/Dissolved Polysulfide Batteries, ChemSusChem. 7 (2014) 2545–2553. doi:10.1002/cssc.201402329.

[53] O.A. Vargas C., Á. Caballero, J. Morales, Can the performance of graphene nanosheets for lithium storage in Li-ion batteries be predicted?, Nanoscale. 4 (2012) 2083. doi:10.1039/c2nr11936f.

[54] Z.-S. Wu, W. Ren, L. Wen, L. Gao, J. Zhao, Z. Chen, G. Zhou, F. Li, H.-M.

Cheng, Graphene Anchored with Co_3O_4 Nanoparticles as Anode of Lithium Ion Batteries with Enhanced Reversible Capacity and Cyclic Performance, ACS Nano. 4 (2010) 3187–3194. doi:10.1021/nn100740x.

[55] A. Benítez, D. Di Lecce, G.A. Elia, Á. Caballero, J. Morales, J. Hassoun, A new lithium-ion battery using 3D-array nanostructured graphene-sulfur cathode and silicon oxide-based anode, ChemSusChem. (2018). doi:10.1002/cssc.201800242.

[56] Q. Pang, X. Liang, C.Y. Kwok, L.F. Nazar, Advances in lithium–sulfur batteries based on multifunctional cathodes and electrolytes, Nat. Energy. 1 (2016) 16132. doi:10.1038/nenergy.2016.132.

[57] L.E. Camacho-Forero, T.W. Smith, P.B. Balbuena, Effects of high and low salt concentration in electrolytes at lithium-metal anode surfaces, J. Phys. Chem. C. 121 (2017) 182–194. doi:10.1021/acs.jpcc.6b10774.

[58] J. Ming, Z. Cao, W. Wahyudi, M. Li, P. Kumar, Y. Wu, J.Y. Hwang, M.N. Hedhili, L. Cavallo, Y.K. Sun, L.J. Li, New Insights on Graphite Anode Stability in Rechargeable Batteries: Li Ion Coordination Structures Prevail over Solid Electrolyte Interphases, ACS Energy Lett. 3 (2018) 335–340. doi:10.1021/acsenergylett.7b01177.

[59] K. Ueno, K. Yoshida, M. Tsuchiya, N. Tachikawa, K. Dokko, M. Watanabe, Glyme-lithium salt equimolar molten mixtures: Concentrated solutions or solvate ionic liquids?, J. Phys. Chem. B. 116 (2012) 11323–11331. doi:10.1021/jp307378j.

[60] B.A. Boukamp, A Nonlinear Least Squares Fit procedure for analysis of immittance data of electrochemical systems, Solid State Ionics. 20 (1986) 31–44. doi:10.1016/0167-2738(86)90031-7.

[61] J. Conder, C. Villevieille, S. Trabesinger, P. Novák, L. Gubler, R. Bouchet,

Electrochemical impedance spectroscopy of a Li–S battery: Part 1. Influence of the electrode and electrolyte compositions on the impedance of symmetric cells, Electrochim. Acta. 244 (2017) 61–68. doi:10.1016/j.electacta.2017.05.041.

[62] L. Carbone, D. Di Lecce, M. Gobet, S. Munoz, M. Devany, S. Greenbaum, J. Hassoun, Relevant Features of a Triethylene Glycol Dimethyl Ether-Based Electrolyte for Application in Lithium Battery, ACS Appl. Mater. Interfaces. 9 (2017) 17085–17095. doi:10.1021/acsami.7b03235.

[63] L. Ji, M. Rao, S. Aloni, L. Wang, E.J. Cairns, Y. Zhang, Porous carbon nanofiber–sulfur composite electrodes for lithium/sulfur cells, Energy Environ. Sci. 4 (2011) 5053. doi:10.1039/c1ee02256c.

[64] L. Carbone, R. Verrelli, M. Gobet, J. Peng, M. Devany, B. Scrosati, S. Greenbaum, J. Hassoun, Insight on the Li_2S electrochemical process in a composite configuration electrode, New J. Chem. 40 (2016) 2935–2943. doi:10.1039/C5NJ03402G.

[65] D. Aurbach, Review of selected electrode–solution interactions which determine the performance of Li and Li ion batteries, J. Power Sources. 89 (2000) 206–218. doi:10.1016/S0378-7753(00)00431-6.

[66] B. Ding, C. Yuan, L. Shen, G. Xu, P. Nie, X. Zhang, Encapsulating Sulfur into Hierarchically Ordered Porous Carbon as a High-Performance Cathode for Lithium-Sulfur Batteries, Chem. - A Eur. J. 19 (2013) 1013–1019. doi:10.1002/chem.201202127.

[67] T.A. Zegeye, M.-C. Tsai, J.-H. Cheng, M.-H. Lin, H.-M. Chen, J. Rick, W.-N. Su, C.-F.J. Kuo, B.-J. Hwang, Controllable embedding of sulfur in high surface area nitrogen doped three dimensional reduced graphene oxide by solution drop

impregnation method for high performance lithium-sulfur batteries, J. Power Sources. 353 (2017) 298–311. doi:10.1016/j.jpowsour.2017.03.063.

[68] Z.-Y. Sui, Q.-S. Yang, H.-Y. Zhou, X. Li, Y.-N. Sun, P.-W. Xiao, Z.-X. Wei, B.-H. Han, Nitrogen-doped graphene aerogel as both a sulfur host and an effective interlayer for high-performance lithium–sulfur batteries, Nanotechnology. 28 (2017) 495701. doi:10.1088/1361-6528/aa91f1.

[69] C. Wang, K. Su, W. Wan, H. Guo, H. Zhou, J. Chen, X. Zhang, Y. Huang, High sulfur loading composite wrapped by 3D nitrogen-doped graphene as a cathode material for lithium–sulfur batteries, J. Mater. Chem. A. 2 (2014) 5018–5023. doi:10.1039/C3TA14921H.

[70] Z. Li, S. Deng, R. Xu, L. Wei, X. Su, M. Wu, Combination of Nitrogen-Doped Graphene with MoS_2 Nanoclusters for Improved Li-S Battery Cathode: Synthetic Effect between 2D Components, Electrochim. Acta. 252 (2017) 200–207. doi:10.1016/j.electacta.2017.09.001.

[71] M. Yu, J. Ma, M. Xie, H. Song, F. Tian, S. Xu, Y. Zhou, B. Li, D. Wu, H. Qiu, R. Wang, Freestanding and Sandwich-Structured Electrode Material with High Areal Mass Loading for Long-Life Lithium-Sulfur Batteries, Adv. Energy Mater. 7 (2017) 1602347. doi:10.1002/aenm.201602347.

[72] L. Li, G. Zhou, L. Yin, N. Koratkar, F. Li, H.M. Cheng, Stabilizing sulfur cathodes using nitrogen-doped graphene as a chemical immobilizer for Li-S batteries, Carbon 108 (2016) 120–126. doi:10.1016/j.carbon.2016.07.008.

[73] F.-F. Zhang, C.-L. Wang, G. Huang, D.-M. Yin, L.-M. Wang, Enhanced electrochemical performance by a three-dimensional interconnected porous nitrogen-doped graphene/carbonized polypyrrole composite for lithium–sulfur

batteries, RSC Adv. 6 (2016) 26264–26270. doi:10.1039/C6RA02667B.

[74] K. Ding, Y. Bu, Q. Liu, T. Li, K. Meng, Y. Wang, Ternary-layered nitrogen-doped graphene/sulfur/ polyaniline nanoarchitecture for the high-performance of lithium–sulfur batteries, J. Mater. Chem. A. 3 (2015) 8022–8027. doi:10.1039/C5TA01195G.

[75] Y. Qiu, W. Li, W. Zhao, G. Li, Y. Hou, M. Liu, L. Zhou, F. Ye, H. Li, Z. Wei, S. Yang, W. Duan, Y. Ye, J. Guo, Y. Zhang, High-Rate, Ultralong Cycle-Life Lithium/Sulfur Batteries Enabled by Nitrogen-Doped Graphene, Nano Lett. 14 (2014) 4821–4827. doi:10.1021/nl5020475.

[76] Z. Wang, Y. Dong, H. Li, Z. Zhao, H. Bin Wu, C. Hao, S. Liu, J. Qiu, X.W. (David) Lou, Enhancing lithium–sulphur battery performance by strongly binding the discharge products on amino-functionalized reduced graphene oxide, Nat. Commun. 5 (2014) 5002. doi:10.1038/ncomms6002.

[77] X. Wang, Z. Zhang, Y. Qu, Y. Lai, J. Li, Nitrogen-doped graphene/sulfur composite as cathode material for high capacity lithium–sulfur batteries, J. Power Sources. 256 (2014) 361–368. doi:10.1016/j.jpowsour.2014.01.093.

[78] J. Hassoun, K.-S. Lee, Y.-K. Sun, B. Scrosati, An Advanced Lithium Ion Battery Based on High Performance Electrode Materials, J. Am. Chem. Soc. 133 (2011) 3139–3143. doi:10.1021/ja110522x.

Table 1

Sample	C=C/C–C 284.8 eV	C–O alkoxy 285.9 eV	C–O epoxy 286.7 eV	C=O carbonyl 288.0 eV	C–O carboxyl 289.0 eV	$\pi \rightarrow \pi^*$ 290.8 eV
GO	38.12 %	--	50.97 %	7.69 %	3.22 %	--
3DNG	63.21 %	17.43 %	8.14 %	4.95 %	3.13 %	3.14 %

Table 1

Table 2

Cell condition	Circuit	R_{i1} / Ω	R_{i2} / Ω	R_{i3} / Ω	χ^2
OCV	$R_e(R_{i,1}Q_{i,1})(R_{i,2}Q_{i,2})Q_3$	44.9 ± 1.0	10 ± 3	-	4.7×10^{-4}
After 6 cycles	$R_e(R_{i,1}Q_{i,1})(R_{i,2}Q_{i,2})Q_3$	6.29 ± 0.06	0.27 ± 0.14	-	4.6×10^{-5}
After 12 cycles	$R_e(R_{i,1}Q_{i,1})(R_{i,2}Q_{i,2})(R_{i,3}Q_{i,3})Q_3$	1.1 ± 0.2	12.4 ± 0.3	2.9 ± 0.3	1.6×10^{-5}

Table 2

Figure 1

Click here to download Figure(s) - provided separately: Figure 1.pdf

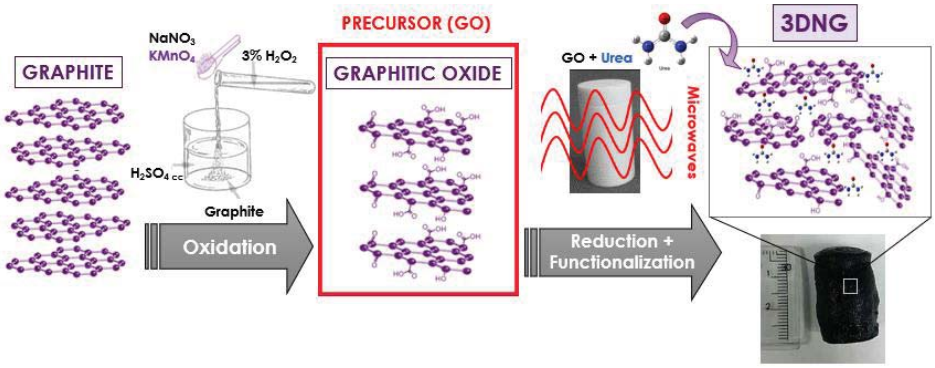

Figure 1

Figure 2

Click here to download Figure(s) - provided separately: Figure 2.pdf

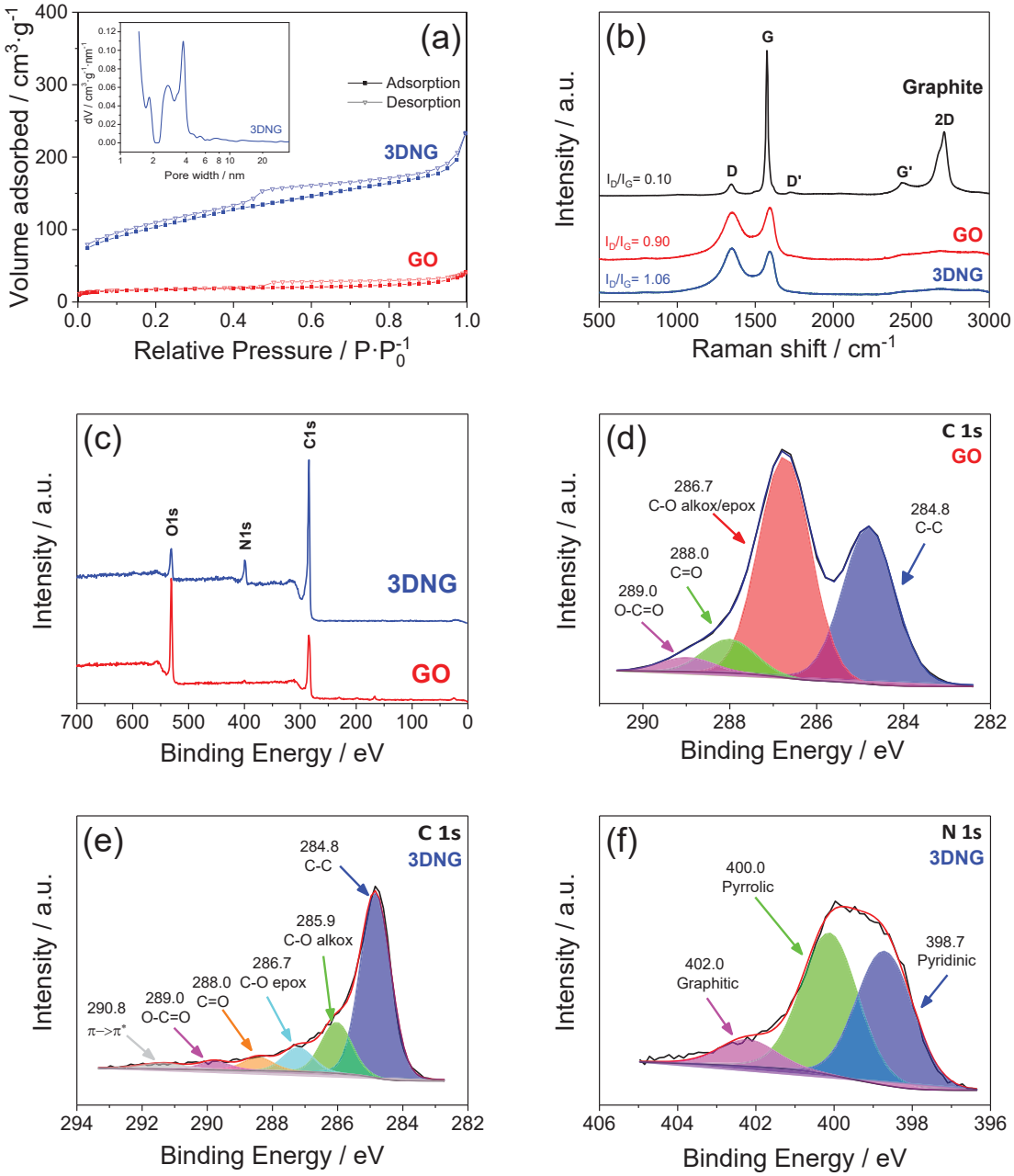

Figure 2

Figure 3
Click here to download Figure(s) - provided separately: Figure 3.pdf

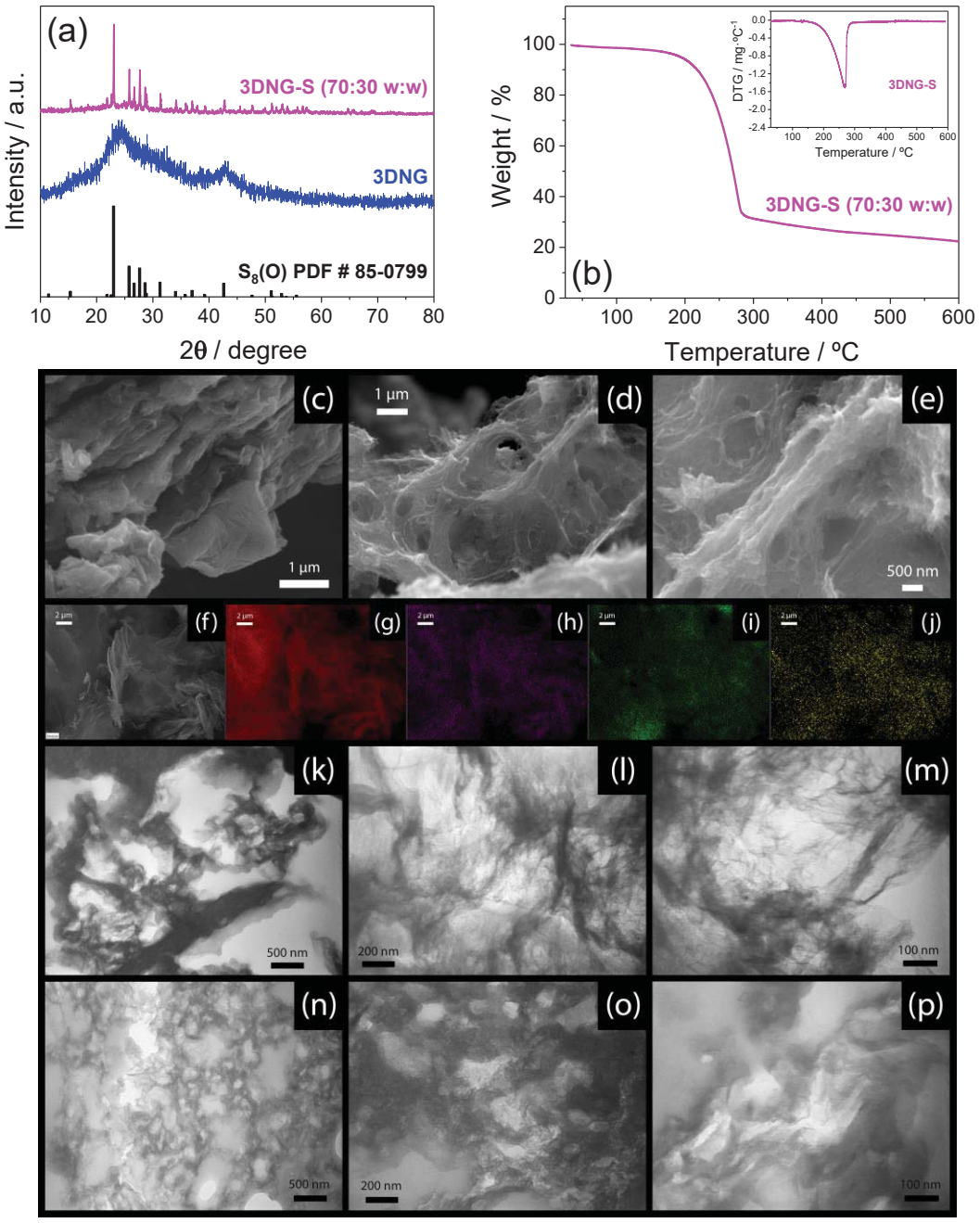

Figure 3

Figure 4

Click here to download Figure(s) - provided separately: Figure 4.pdf

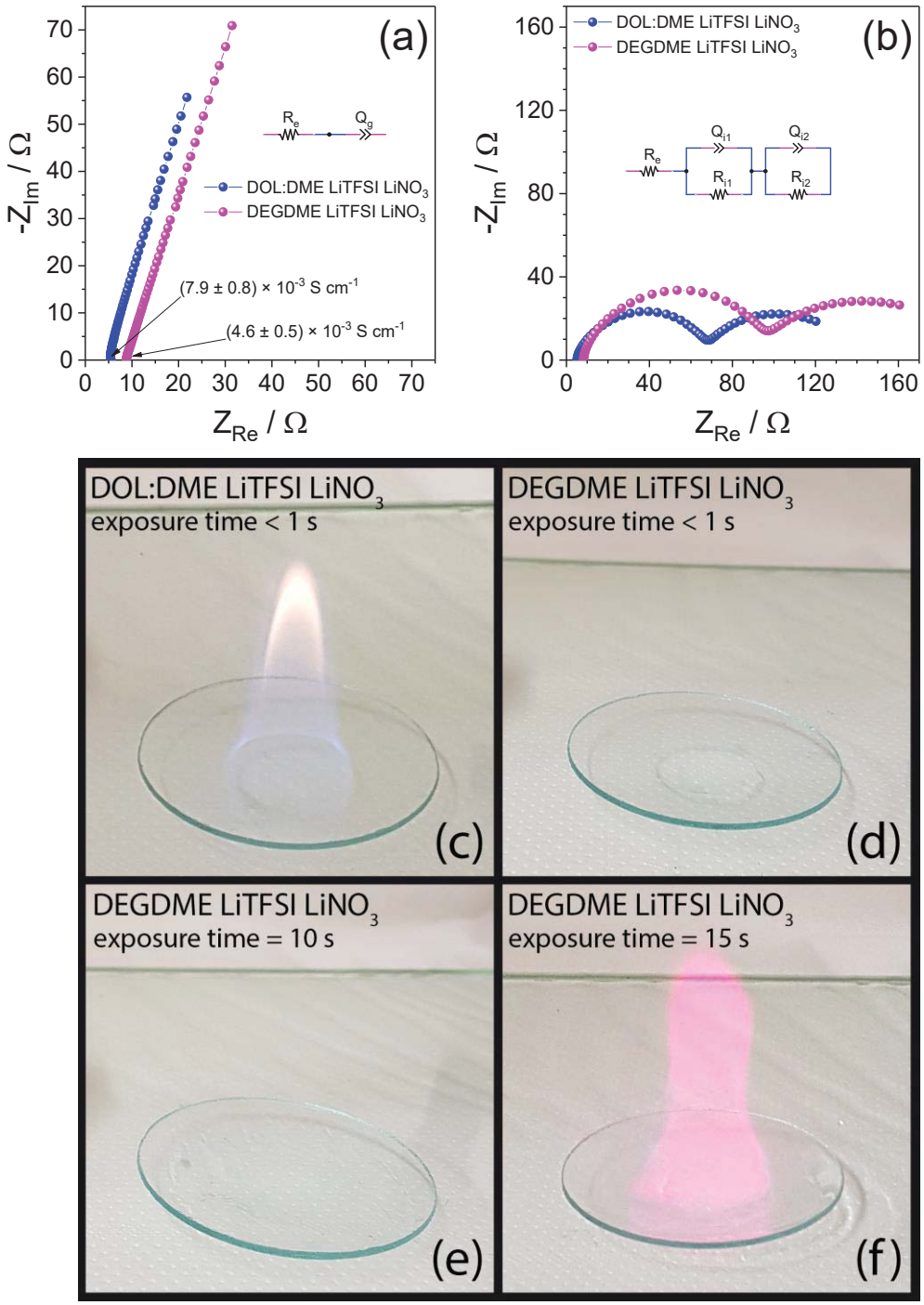

Figure 4

Figure 5

Click here to download Figure(s) - provided separately: Figure 5.pdf

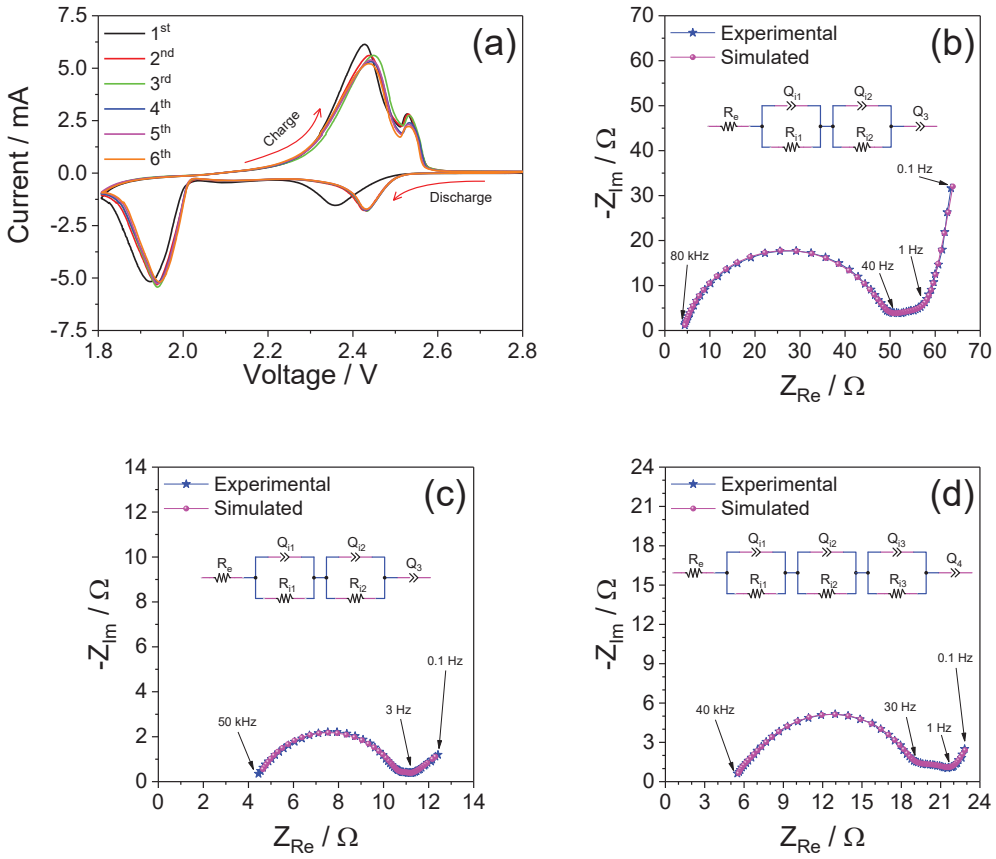

Figure 5

Figure 6

Click here to download Figure(s) - provided separately: Figure 6.pdf

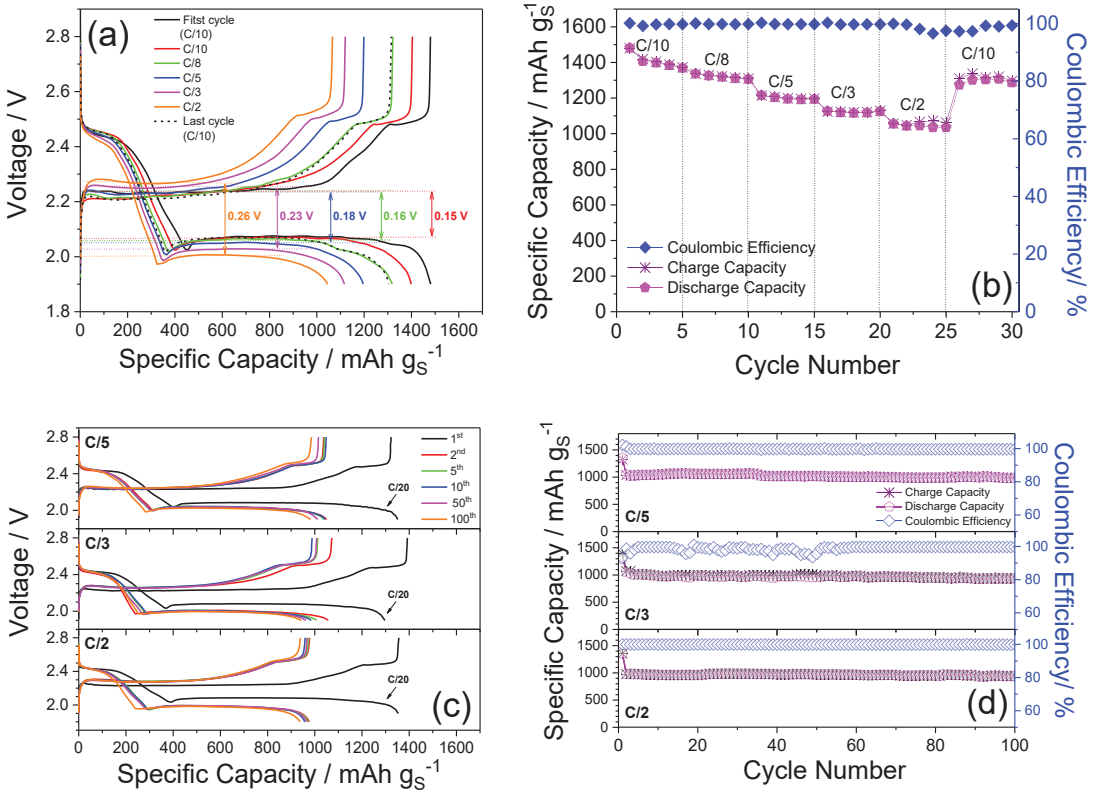

Figure 6

Table captions

Table 1. Percent contribution of the six components used in the fitting of the C1s photoemission peak of GO and 3DNG samples (see Figure 1b-d and the related discussion).

Table 2. Results of NLLS analyses [51] performed on the impedance spectra of Fig. 4b-c, recorded upon cyclic voltammetry of the Li/DEGDME-LiTFSI-$LiNO_3$/3DNG-S cell at the OCV, after 6 and after 12 cycles. In detail: employed equivalent circuit, interphase resistance and χ^2 value of the fit. See experimental section for samples' acronym.

Figure captions

Figure 1. Synthesis pathway of the 3DNG-S material, including a photograph of the 3DNG-S monolith after the microwave-assisted solvothermal treatment. See experimental section for samples' acronym.

Figure 2. (a) N_2 adsorption/desorption isotherms of GO and 3DNG samples; figure inset: pore size distribution calculated by the DFT model applied to 3DNG. **(b)** Raman spectra of graphite, GO and 3DNG. **(c)** XPS spectra of GO and 3DNG. **(d)** XPS spectra for the C 1s photoemission peak of GO. **(e, f)** XPS for the **(e)** C 1s photoemission peak and **(f)** N 1s photoemission peak of 3DNG sample. See experimental section for samples' acronym.

Figure 3. (a) XRD patterns of the 3DNG and 3DNG-S samples; reference data sheet of crystalline S (PDF # 85-0799). **(b)** TGA trace of 3DNG-S composite under a N_2 flow upon heating at 5 ºC min^{-1}; DTG curve in figure inset. **(c-l)** Electron microscopy analysis of the samples. In detail: **(c-e)** SEM images of **(c)** GO and **(d, e)** 3DNG; **(f)** SEM image and **(g-l)** related SEM-EDS elemental maps of **(g)** C, **(h)** O, **(i)** S and **(j)** N for the 3DNG-S composite; **(k-p)** TEM images at several magnifications of **(k-m)** 3DNG and **(n-p)** 3DNG-S. See experimental section for samples' acronym.

Figure 4. (a, b) Impedance spectra of symmetrical **(a)** SS/SS and **(b)** Li/Li cells using DEGDME-LiTFSI-$LiNO_3$ electrolyte and DOL:DME-LiTFSI-$LiNO_3$ reference solution; equivalent circuits used for NLLS fit [51] of the spectra are reported in inset; ionic conductivities are calculated by taking the EIS responses of panel **a** (see the experimental for further details). **(c-f)** Flammability tests of **(c)** DOL:DME-LiTFSI-$LiNO_3$ reference and **(d-f)** DEGDME-LiTFSI-$LiNO_3$ electrolyte through direct exposure to a butane flame. In detail: **(c)** flame evolution in DOL:DME-LiTFSI-$LiNO_3$ after exposure time < 1 s (direct ignition); **(d, e)** absence of flame in DEGDME-LiTFSI-$LiNO_3$ after **(d)** exposure

time < 1s and **(e)** exposure time = 10 s; **(f)** flame evolution in DEGDME-LiTFSI-$LiNO_3$ after exposure time = 15 s. See experimental section for samples' acronym.

Figure 5. (a) Cyclic voltammetry of Li/DEGDME-LiTFSI-$LiNO_3$/3DNG-S cell at a scan rate of 0.1 mV s^{-1}. **(b-d)** Impedance spectra of the cell **(b)** at the OCV, **(c)** after 6 and **(d)** after 12 voltammetry cycles; equivalent circuits used for NLLS fit [51] of the spectra are reported in inset. See experimental section for samples' acronym.

Figure 6. (a, b) Rate capability test in terms of **(a)** voltage profile and **(b)** galvanostatic cycling behavior performed at C/10, C/8, C/5, C/3 and C/2 rates of the Li/DEGDME-LiTFSI-$LiNO_3$/3DNG-S cell. **(c, d)** Galvanostatic tests at C/5, C/3 and C/2 in terms of **(c)** voltage profiles and **(d)** cycling behavior. Voltage range: 1.9 – 2.8 V. 1C = 1675 mA g_S^{-1}. See experimental section for samples' acronym.